POLITECNICO DI TORINO
Repository ISTITUZIONALE

Synergistic freshwater and electricity production using passive membrane distillation and waste heat recovered from camouflaged photovoltaic modules

(Article begins on next page)

10 April 2024

Synergistic freshwater and electricity production using passive membrane distillation and waste heat recovered from camouflaged photovoltaic modules

Giovanni Antonetto[a], Matteo Morciano[a,b], Matteo Alberghini[a,b], Gabriele Malgaroli[a], Alessandro Ciocia[a], Luca Bergamasco[a], Filippo Spertino[a], Matteo Fasano[a,b,*]

[a]*Department of Energy, Politecnico di Torino, Corso Duca degli Abruzzi 24, 10129 Torino, Italy*
[b]*Clean Water Center, Politecnico di Torino, Corso Duca degli Abruzzi 24, 10129 Torino, Italy*

Abstract

A sustainable supply of both freshwater and energy is key for modern societies. In this work, we investigate a synergistic way to address both these issues, producing freshwater while reducing greenhouse gas emissions due to electricity generation. To this, we propose a coupling between a photovoltaic (PV) device and an innovative desalination technique based on passive multi-stage membrane distillation. The passive distillation device is driven by low-temperature heat and does not need any mechanical or electrical devices to operate. The required heat is recovered from the back side of the PV device that, for the first time, mitigates the aesthetic and environmental impact thanks to an innovative surface texture. The aim is to demonstrate the feasibility to generate PV electricity from the sun and, simultaneously, freshwater from the waste heat. The solution is studied by numerical simulations and experiments at the same time, achieving a good accordance between these two approaches. The device is able to produce up to 2 L m^{-2} h^{-1} of freshwater under one sun irradiance. Furthermore, a relative photovoltaic efficiency gain of 4.5% is obtained, since the temperature of the PV module is reduced by 9 °C when coupled with the desalination technology. This work paves the way to compact installations made of such passive units, which may easily provide energy and safe water with low environmental and visual impact, especially in off-grid areas and emergency conditions.

Keywords: Solar energy, Passive desalination, Membrane distillation, Waste heat recovery, Photovoltaic, Electricity generation

Nomenclature

Greek letters

β, γ	Temperature coefficients	-
ϵ_m	Membrane porosity	-
η_dist	Efficiency of the distillation device	-
η_PV	PV panel efficiency	-
η_v	Dynamic viscosity of the gas mixture	Pa s
μ_i	Chemical potential of species i	J mol^{-1}
σ	Stefan-Boltzmann constant	W m^{-2} K^{-4}
τ	Membrane tortuosity	-

Symbols

ε	Optical emissivity	-
$\bar{T}$	Average membrane temperature	K
Δh_LV	Heat of water vaporization	J kg^{-1}
A	Surface area	m^2
a	Activity coefficient	-
C	Electrical capacitance	F
d_a	Air gap thickness	m
d_p	Average membrane pores diameter	m
d_z	Membrane thickness	m
$D_{i\mathrm{K}}$	Knudsen diffusion for species i	m^2 s^{-1}
D_{ij}	Molecular diffusion for species i in j	m^2 s^{-1}

*Corresponding author
Email address: `matteo.fasano@polito.it` (Matteo Fasano)

I	Electrical current	A
I_{rr}	Solar irradiance	$\mathrm{W\,m^{-2}}$
J	Specific mass flow rate	$\mathrm{kg\,m^{-2}\,s^{-1}}$
K	Membrane permeability	$\mathrm{kg\,Pa^{-1}m^{-2}s^{-1}}$
K_{v}	Viscous permeabilty coefficient	$\mathrm{m^2}$
m_{w}	Molar mass of water	$\mathrm{kg\,mol^{-1}}$
M_i	Molar flux of species i	$\mathrm{mol\,m^{-2}\,s^{-1}}$
$N_{\mathrm{p/s}}$	Number of PV strings in parallel/series	-
P	Electrical power	W
p	Absolute pressure	Pa
P_{mpp}	PV power output at the Maximum Power Point	W
q_{in}	Specific heat flux	$\mathrm{W\,m^{-2}}$
R	Universal gas constant	$\mathrm{J\,K^{-1}\,mol^{-1}}$
T	Temperature	°C
U	Effective thermal transmittance	$\mathrm{W\,m^{-2}\,K^{-1}}$
V	Voltage	V
x_i	Molar fraction of species i	-
Y	Mass fraction of the salt solution	-
z	Vertical coordinate	m

Subscripts and superscripts

a	Air property
amb	Ambient property
cell, n	Property of the PV panel *n-th* cell
cond, n	Property evaluated at the *n-th* condenser
dist	Distiller property
eva, n	Property evaluated at the *n-th* evaporator
exp	Experimental quantity
int	Property of the air gap - membrane interface
oc	Open-circuit
panel	PV panel property
sc	Short-circuit
sim	Simulation quantity
w	Water vapour property
wb	Saltwater basin property

1. Introduction

At the time of writing, more than 1.42 billion people live in areas facing severe water stress all over the world. Despite the significant technological advancements in the last decades, today still less than 3 per cent of the global water resources is safely drinkable. Moreover, given the expected population growth and increasing urbanization in the next years, the global freshwater demand is estimated to increase by 20 to 30 per cent by 2050 in a range of different sectors (UNICEF, March 2021). The second major problem associated with the current projections for global development relates to the increasing demand of energy, and to the consequent potential effect on climate change (De Angelis et al., 2021). Mitigation policies foresee an increasing use of renewable energy sources, towards a global sustainable development and an equal access to energy and freshwater sources (UN General Assembly, 2015).

In this view, water treatment technologies driven by renewable energy sources have great potential towards the above mentioned goals and have been extensively investigated and continuously improved in the recent years (Giudici et al., 2019; Bologna et al., 2020; Nassrullah et al., 2020; Yusuf et al., 2020). In particular, several articles proposed the coupling of photovoltaic (PV) modules with traditional water treatment technologies such as reverse and forward osmosis (Koutroulis and Kolokotsa, 2010; Khayet et al., 2016; Lee et al., 2016), electrodialysis (Campione et al., 2018; Xu et al., 2020) and mechanical vapour compression hybrid systems (Helal and Al-Malek, 2006). However, most of the proposed integrated systems use PV modules to power conventional desalination devices, while only a few works have experimentally investigated the coupling of PV with desalination devices (Manokar et al., 2018; Abd Elbar et al., 2019; Elminshawy et al., 2020; Chen et al., 2021), proving the complexity of this objective. Recently, novel advanced materials paved the way for passive devices in the field of simultaneous freshwater and electricity production (Liu et al., 2020; Dao et al., 2021). Passive technologies have the particular advantage to: i) include no moving mechanical parts, thus typically requiring low maintenance and associated costs; ii) be especially suitable for operation in off-grid areas, where no connection to the electric power grid is available. Among the others, promising results were obtained by bio-inspired systems (Jiang et al., 2020; Zhou et al., 2020), advanced nano-structured materials (Xue et al., 2017; Zhang et al., 2020), traditional (Wang et al., 2019, 2021) and advanced (Yang et al., 2017) membrane technologies. However, the novelty of these materi-

als and the current fabrication techniques relegate these technologies to lab-scale and centimetre-sized prototypes with a low power density output, thus still lacking cost-effectiveness and a comprehensive evaluation of their scalability on a device-scale perspective.

The coupling of PV and multi-stage passive devices, a technology based on membrane distillation recently reported by some of the authors of the present work (Chiavazzo et al., 2018), offers a good compromise between modularity, scalability, low cost and high productivity. The device operates at ambient pressure using a multi-stage rationale, where high efficiency is obtained thanks to a series of multiple evaporation and condensation stages where latent heat is recovered several times (Signorato et al., 2020). The water feeding relies on capillary action, which makes it free from moving mechanical parts and additional energy needs. Thus, the design results to be completely passive, compact, and the employed materials inexpensive. While in the original concept solar thermal energy was exploited to power the system, the required low-temperature thermal energy may be also recovered from other sources of wasteheat (Morciano et al., 2020a).

Based on this idea, in this work we propose a coupled solution for efficient and sustainable freshwater and electricity production. The above mentioned multistage distillation device is indeed coupled with a PV module. The desalination unit is integrated on the back side of the PV unit, which provides the wasteheat to empower the distillation stages. This latter energy recovery has the additional advantage to lower the working temperature of the PV module, thus increasing its conversion efficiency (Letcher and Fthenakis, 2018). While similar integrated solutions have already been explored (Manokar et al., 2018; Sultan and Efzan, 2018; Wang et al., 2019), here we address the additional problem related to the environmental and visual impact of PV installations (Sánchez-Pantoja et al., 2018; Al-Karaghouli et al., 2010). To this, we propose and investigate the performance of a PV module with an innovative aesthetic surface coating, which allows to reduce the impact with the surrounding landscape. The resulting compact unit results to be particularly suitable for floating installations (Sahu et al., 2016; Cazzaniga et al., 2018). In order to assess the proposed solution, here we experimentally tested the performance of a working prototype. A numerical model is also developed and compared with the experimental results, to provide deeper insight on the sensitivity to the operating conditions.

The article is organized as follows. The working principle of the multi-stage desalination unit and its integration with the PV module are outlined in Section 2.

Section 3 reports on the experimental setup for testing the performance of the prototype. The modeling approach and the adopted numerical framework are discussed in Section 4; whereas, the results are reported in Section 5. Finally, the conclusions are drawn in Section 6, along with the perspective developments of the proposed work.

2. Materials

2.1. Passive membrane distillation unit

The adopted multi-stage membrane distillation unit powered by solar thermal energy was originally introduced by Chiavazzo et al. (2018). It consists of a series of identical stages, which allow to recover the latent heat of vaporization several times before it is evacuated to the environment. A schematics of the working principle is reported in Fig. 1a. Each stage consists of: a synthetic microfiber (hydrophilic) cloth, acting as evaporator; a 0.1 μm microporous polytetrafluoroethylene (hydrophobic) membrane, which separates the saltwater side from the distillate side; a second hydrophilic cloth, acting as condenser. The different stages are separated by an aluminum sheet, to ease heat recovery and transfer to the next stage. Saltwater feeding is provided by the capillary action from the hydrophilic cloths in each stage, whereas the distillate water discharge is driven by gravity. The external parts of the cloths are sealed in plastic films, to avoid evaporation to the ambient. Low-temperature thermal energy drives the distillation process through the stages, and an (aluminum) heat sink evacuates the waste heat to the surrounding environment at the final stage. In this case, the low-grade thermal energy feeding comes from the waste heat recovered from the PV module. During daytime operation, the recovered heat induces a temperature gradient between the saltwater in the evaporator and the freshwater in the condenser of the first stage. This results in a gradient of the partial pressures of water vapor between the cloths, which generates a net vapor flux across the hydrophobic membrane (preventing accidental liquid water flow and mixing, instead). The distilled liquid in the condenser is then discharged into the freshwater basin by gravity; the latent head released from condensation triggers the same process in the next stage via the aluminum sheet. During nighttime (see Fig. 1b), the salt accumulated during daytime operation spontaneously diffuses from the evaporators back to the saltwater basin due to the salinity gradient (Morciano et al., 2020b). In order to ease this self-cleaning process, the assembly and dimensions of each evaporator and condenser cloth are designed to minimize the salt diffusion path back to the saltwater basin (see the final assembly and the related exploded view in Fig. 1c and 1d, respectively). In this case, the dimensions of each evaporator cloth are 125 mm × 35 mm, while those of each condenser are 125 mm × 25 mm. In this configuration, the salt diffusion distance is minimized (i.e. 35/2 = 17.5 mm) with respect to the longitudinal length of the final assembly.

2.2. Camouflaged photovoltaic unit

The photovoltaic (PV) system consists of a 4-cells mono-crystalline silicon (c-Si) solar module, placed into a semi-flexible, lightweight panel (XDISC® ASole-13) with an innovative aesthetic surface coating patented by ILOOXS (see Fig. 1e). In this case, the chosen coating represents a rippled surface of blue marine water, which is meant to reduce the visual impact with the surrounding landscape in case of floating installation.

2.3. Integrated unit for freshwater and electricity production

The tested prototype consists of the camouflaged PV panel and eight passive desalination modules (each one made of three distillation stages), which are allocated in a tailored structure according to the schematics reported in Fig. 2. Two distillation modules are positioned underneath each of the four cells of the PV panel. The structure, distillate containers and frames are custom made in plastic. The overall structure is clamped using screws, and the resulting final dimensions of the prototype are 488 mm × 350 mm × 48.5 mm. It is worth to point out that, besides structural purposes, the plastic frame also serves to avoid overloading of the distillation stages and thus accidental exceeding of the liquid entry pressure (LEP) for the membrane. The containing structure presents different openings at the bottom, in order to allow the cloths and the heat sinks to dip in the saltwater bath beneath. The distillate basins in the plastic case are insulated and protected from saltwater contamination. This design would allow the prototype to float above seawater or to be installed onshore (with a proper refill of saltwater in the basin). Detailed information on the design and manufacturing of the plastic frame can be found in the Supplementary note 1.

3. Experimental methods

3.1. Setup for testing the distiller

A schematic of the experimental setup used to test and characterize a single distiller module is shown in
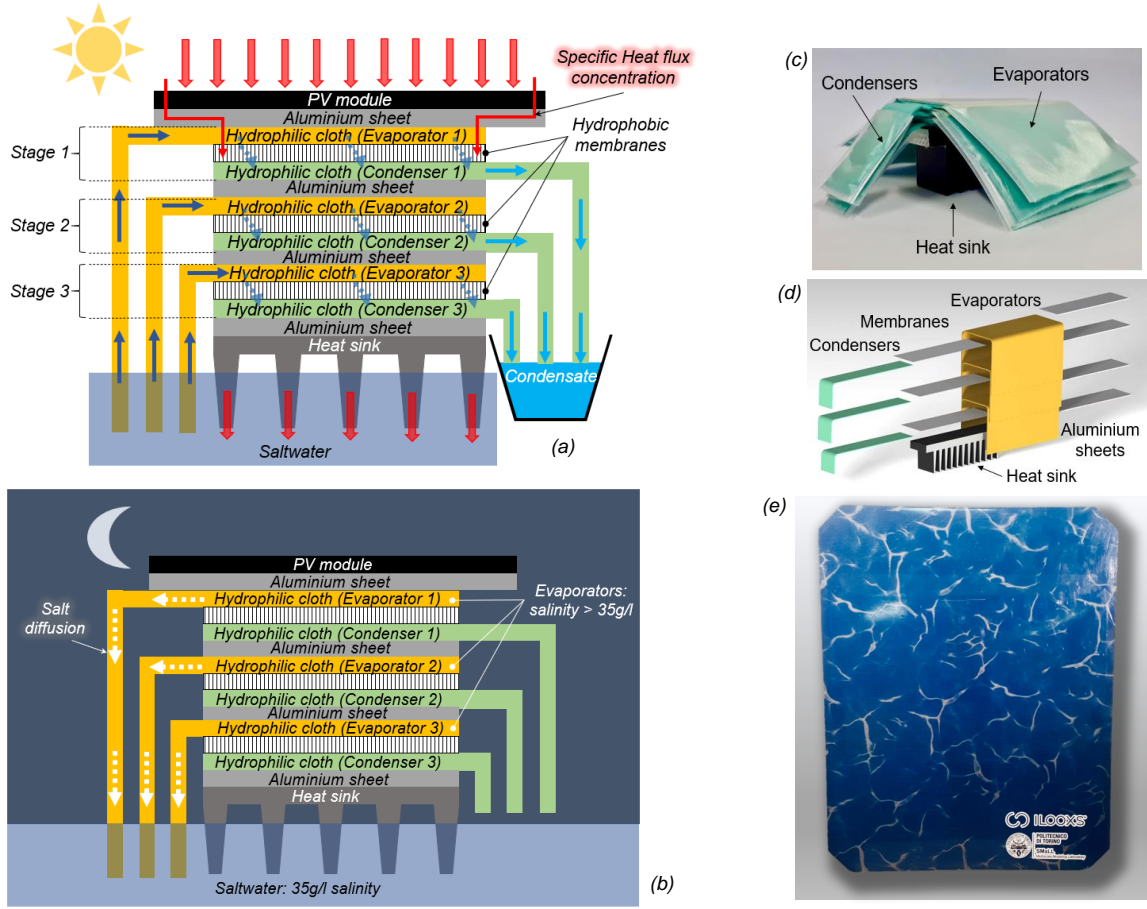
Figure 1: Scheme of the photovoltaic module and the passive multi-stage membrane distillation system. (a) Components and heat and mass flows during daytime operation; (b) autonomous rinsing during nighttime; (c) picture of the 3-stages passive distiller; (d) exploded view rendering of the 3-stages passive distiller; (e) PV module with aesthetic camouflage used in this work.

Fig. 3. The module is fed with the waste heat from the back side of the PV panel. The specific mass flow rate (J) of distilled water, expressed in L m^{-2} h^{-1}, is evaluated under the reference conditions of irradiance I_{rr} equal to one sun, namely I_{rr} = 1000 W m^{-2}; salinity and temperature of the sodium chloride solution are equal to 35 g L^{-1} and 20 °C, respectively. In these tests, the PV module is unplugged, thus acting only as a photo-thermal device without delivering any current.

The distiller is positioned in the tailored plastic case and the PV panel is installed on the top (see Supplementary note 1). A solar simulator (infinityPV ISOSun) is used to mimic the sun irradiance. The extremities of each evaporator cloth are dipped in the saltwater together with the fins of the heat sink, whilst the ends of each condenser cloth spill the distillate in a container positioned on a precision scale (Radwag PS100.R2). The recorded weight of the distillate basin allows to cal-

culate the specific mass flow rate of distillate J produced by the distiller. In order to guarantee a constant temperature of feeding water, a cooling circuit connected to a heat exchanger (Julabo Corio CD with refrigerated bath Julabo 300F) is adopted. Five K-thermocouples (RS-PRO) connected to a Data Acquisition System – DAQ (NI cDAQ-9174) are used to measure the temperature of: the back side of the PV panel next to the contact area with the distiller (T_{panel}); the first evaporator ($T_{eva,1}$); the last condenser ($T_{cond,3}$); the saltwater in the basin (T_{wb}); the air above the panel (T_{amb}). A refractometer (Hannah Instruments HI 96821) is used to measure the salinity of water solutions. A pyranometer (Delta OHM LP PYRA 08) is employed to set the irradiance of the sun simulator at the required value before starting the experimental campaign. During the experiments, infrared pictures of the various components are taken with a thermal camera (FLIR TG167).
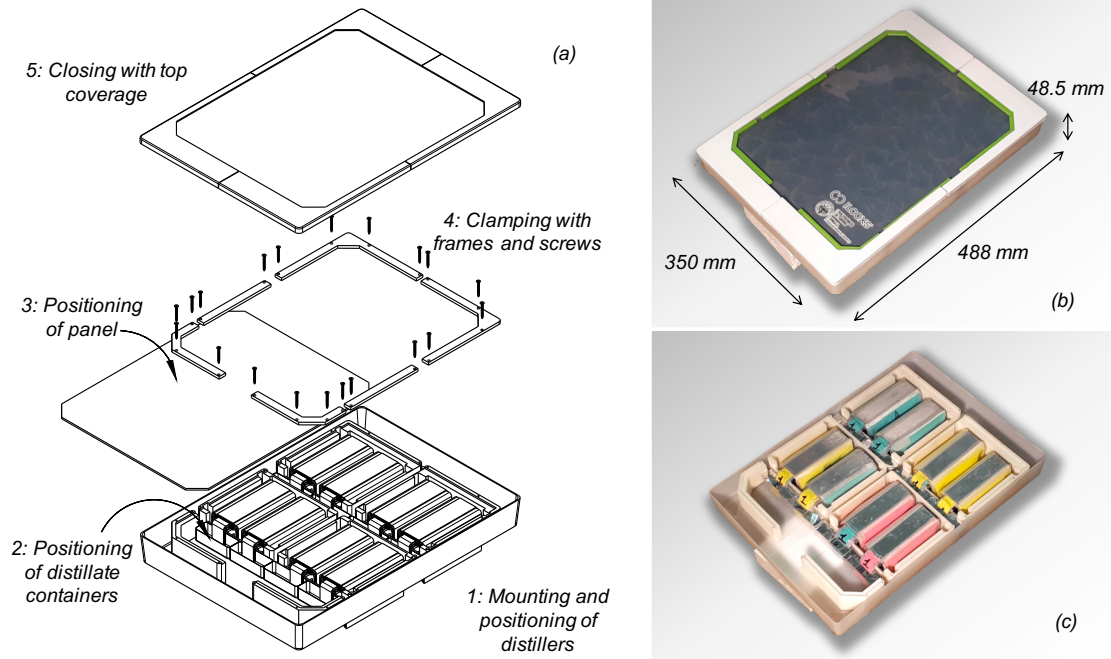
Figure 2: Integrated solution: passive 3-stage distillers and camouflaged PV module. (a) Exploded view with mounting operations; pictures of (b) closed and (c) open configuration. In panel (c), the four sectors in which the eight distillers are fitted can be distinguished. In detail, each sector hosts two distillers. This design is conceived to maximize the contact between the back surface of the PV and the top face of distillers.

Before and after the test, the salinity of the produced distillate is checked to ensure that no salt contamination has occurred. After each trial, the salinity in different points on each condenser cloth is measured, to further ensure that no salt contamination has occurred.

3.2. Setup for testing the entire prototype

The experimental setup adopted to test the full prototype, consisting of the eight distillers and the unplugged PV module, is similar to that described in the previous Section 3.1 and it is shown in Fig. 4.

The increased complexity of the system, due to the simultaneous operation of the eight distillers, allows to measure only the total distillate production of all the modules. In addition, these experiments are designed to evaluate the temperature decrease of the PV cells when mounted together with the distillers. The testing conditions are the same as those described in Section 3.1, namely incoming irradiance equal to $I_{rr} = 1000$ W m^{-2}, salinity and temperature of the sodium chloride solution equal to 35 g L^{-1} and 20 °C, respectively.

The thermocouples are positioned to measure the following temperatures: central portion of the bottom side of cells 1 and 4, $T_{cell,1}$ and $T_{cell,4}$; air above the panel, T_{amb}; saltwater in the basin, T_{wb}; first evaporator, $T_{eva,1}$ and last condenser, $T_{cond,3}$, of distillers A, B, G and H

(see Fig. 4). With these measured values it is possible to (i) evaluate the temperature distribution throughout the panel, i.e. how effective is the cooling effect provided by the distillers on the PV cells, and to (ii) calculate the temperature gradients that drive the distillation processes.

Before starting the experiments, each distillate basin is filled with 9 mL of freshwater, in order to dip the extremities of the condenser cloths and facilitate initial distillate collection. The weight of the produced freshwater is measured before and after the test. The salinity of saltwater is checked before and after each test, whilst the salinity of the distillate is checked at the end of the trial. The duration of the experiments is up to 4 h.

3.3. Electrical characterization of the PV module

The experimental setup used to evaluate the electrical characteristics of the selected PV module is shown in Fig. 5. The current-voltage $(I - V)$, the power-voltage $(P - V)$ curves, together with the PV efficiency (η_{PV}) are strictly dependent on the solar irradiance I_{rr} and on the temperature of the cell T_{cell} (Solanki, 2015); thus, they need to be characterized.

Tests have been conducted outdoor, by exposing the PV module to direct sunlight. The experiment has been carried out from 12 a.m. until 2 p.m. during a clear
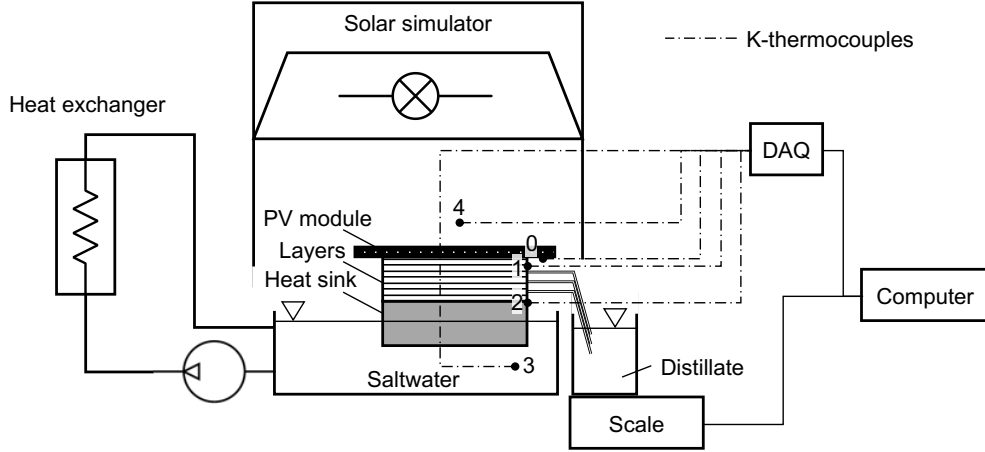
Figure 3: Experimental setup for measuring the distillation performance of a single distiller. The channels of the DAQ collect the signals from the K-thermocouples for the temperature of: back side of the panel, T_{panel} (indicated with 0); first evaporator, $T_{eva,1}$ (indicated with 1); last condenser, $T_{cond,3}$ (indicated with 2); saltwater in the basin, T_{wb} (indicated with 3); air above the panel, T_{amb} (indicated with 4).

sunny day, which has allowed to provide high and stable values of solar irradiance. The temperature of the cell has been regulated at different values to get different $I - V$ and $P - V$ curves. The determination of the $I-V$ curves of PV modules is performed using an Automatic Data Acquisition System (ADAS), see Fig. 5a, which allows to store simultaneously the irradiance I_{rr}, the air temperature T_a and the current I and voltage V waveforms. The measurements are performed using a capacitor, which is initially discharged. Then, the PV module supplies the capacitive load from short-circuit to open-circuit configurations (Spertino et al., 2014, 2015, 2019). According to Spertino et al. (2015), the duration of the capacitor transient t is a function of the short-circuit current I_{sc}, the open-circuit voltage V_{oc}, the number of PV strings in parallel N_p, the number of PV modules in series N_s and the capacitance C of the capacitor according to the following expression:

$$t = 1.82 \cdot C \cdot \frac{N_s V_{oc}}{N_p I_{sc}}, \qquad (1)$$

being in this case $N_s = 1$ and $N_p = 1$, as only one module is tested. The ADAS is periodically calibrated, and it consists of the following components: a notebook PC with a LabVIEW software to emulate a digital oscilloscope; a multifunction data acquisition board with one A/D converter (successive approximation, 16 bit-resolution, sampling rate up to 1.25 MSa s^{-1}, maximum input of $\pm$10 V) and multiplexer; a differential voltage probe with 20:1 attenuation ratio for voltage levels up to 100 V; two current probes (Hall effect) with output sensitivity of 100 mV A^{-1} for current values up to $\pm$30 A, one to measure current and one acting like a trigger

source; a monocrystalline silicon cell for the measurement of I_{rr}; a thermometer, which measures T_a; a capacitive load with capacitance $C = 10$ mF, resulting in a duration of the capacitor transient of about 0.2 s. The uncertainties on measurements have been evaluated as: $\pm$ 0.1% for the voltage, 1% for the current, 1% for the power, 20 W m^{-2} for the irradiance and 0.2 °C for the ambient temperature.

The regulation of the temperature of the cell has been obtained by sticking the PV module on a cooling plate, see Fig. 5b. The cooling plate is fed by water flowing in a closed circuit, cooled by a heat exchanger (Julabo Corio CD with refrigerated bath Julabo 300F). The temperature of each of the four cells is measured with K-thermocouples, located on the back side, and recorded by the DAQ. Acting on the heat exchanger while checking the mean temperature of the cells T_{cell}, steps of $\approx$ +10 °C have been performed from 25 °C up to 65 °C, and for each step the corresponding $I - V$ curve has been recorded. The $P - V$ curves are obtained as indirect measurements of the $I - V$ curves, recalling that $P = IV$. The photovoltaic efficiency is the maximum power P_{mpp} related to the incoming irradiance I_{rr} and overall area of the cells $A_{cells} = 625$ cm^2, i.e. $\eta_{PV} = P_{mpp}/(I_{rr}A_{cells})$. The dependency of the open-circuit voltage V_{oc} with temperature is described via a temperature coefficient β, whereas the dependency for both maximum power P_{mpp} and efficiency is determined by a temperature coefficient γ. The results of the outdoor tests are necessary to calculate β and γ (see Supplementary note 2 for details).
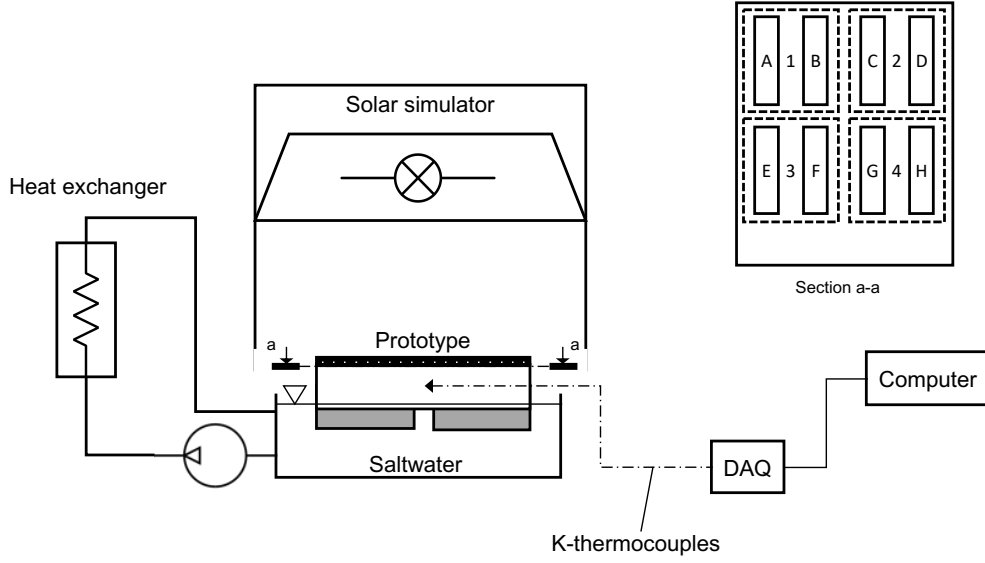
Figure 4: Experimental setup for measuring the distillation performance of the eight distillers on the back side of the PV panel, with detailed nomenclature of the PV cells in contact with the distillers. PV cells are named with numbers (1, 2, 3, 4), whilst distillers with capital letters (A, B, C, D, E, F, G, H). The DAQ collects the signals from the K-thermocouples for the following temperatures of distillers A, B, G and H: central portion of the bottom side of the cells 1 and 4, $T_{\text{cell},1}$ and $T_{\text{cell},4}$; air above the panel, T_{amb}; saltwater in the basin, T_{wb}; first evaporator, $T_{\text{eva},1}$ and last condenser, $T_{\text{cond},3}$.

4. Modelling

4.1. Analytical model

The Maxwell-Stefan equations combined with the Dusty Gas Model are used to describe the mass transfer of multi-components mixture of gases through porous media, such as membranes or air gaps. The model equation can be written as (Chiavazzo et al., 2018; Alberghini et al., 2020; Morciano et al., 2020a):

$$-\frac{x_i}{R\bar{T}}\frac{d\mu_i}{dz} = \frac{x_i K_{\text{v}}\tau}{\eta_{\text{v}}\epsilon_{\text{m}}D_{iK}}\frac{dp}{dz}$$
$$+ \sum_{\substack{j=1 \\ j\neq i}}^{n}\left(\frac{x_j M_i - x_i M_j}{\frac{p\epsilon_{\text{m}}D_{ij}}{R\bar{T}\tau}}\right) + \frac{M_i}{\frac{p\epsilon_{\text{m}}D_{iK}}{R\bar{T}\tau}}, \quad (2)$$

where p and $\bar{T}$ are the absolute pressure and mean temperature within the membrane; R is the universal gas constant; x_i, μ_i and M_i are the molar fraction, chemical potential and molar flux of species i, respectively; ϵ_{m} and τ are the medium porosity and tortuosity, respectively; D_{iK} is the Knudsen diffusion coefficient for species i while D_{ij} is the molecular diffusion coefficient for species i in j; K_{v} is the viscous permeability coefficient and η_{v} the dynamic viscosity of the gas mixture; z is the coordinate along the thickness of the membrane.

The term on the left-hand side of Eq. (2) represents the chemical potential, which acts as driving force for species i. On the right-hand side, the first term represents the viscous flow driven by the absolute pressure gradient across the membrane. The second term represents the molecular diffusion, while the third the Knudsen diffusion. In short, molecular diffusion is a flow regime dictated by losses due to molecule-molecule interactions, while in Knudsen diffusion the losses are due to molecule-wall interactions (Khayet and Matsuura, 2011). Equation (2) can be simplified since a mixture of two ideal gases is considered, namely air (a) and water vapour (w) (Chiavazzo et al., 2018; Morciano et al., 2020a). Owing to the latter assumption $\mu_{\text{w}} = \mu_{\text{w}}^0 + R\bar{T}\ln x_{\text{w}}$, where μ_{w}^0 is the chemical potential of pure water. Hence $\frac{d\mu_{\text{w}}}{dz} = \frac{R\bar{T}}{x_{\text{w}}}\frac{dx_{\text{w}}}{dz}$. Moreover, the distiller works at ambient pressure, so the viscous term $\frac{dP}{dz} = 0$ disappears. Finally, the air is assumed to be stationary inside the membrane since water has a low solubility in air, hence $M_{\text{a}} = 0$. The simplified equation then reads as:

$$-\frac{dx_{\text{w}}}{dz} = \frac{R\bar{T}\tau J\left(1 - x_{\text{w}} + \frac{D_{\text{wa}}}{D_{\text{wK}}}\right)}{p\epsilon_{\text{m}}D_{\text{wa}}m_{\text{w}}}, \quad (3)$$

where m_{w} is the molar mass of water. Equation (3) can be integrated within the membrane and air gap, considering appropriate boundary conditions (see Chiavazzo
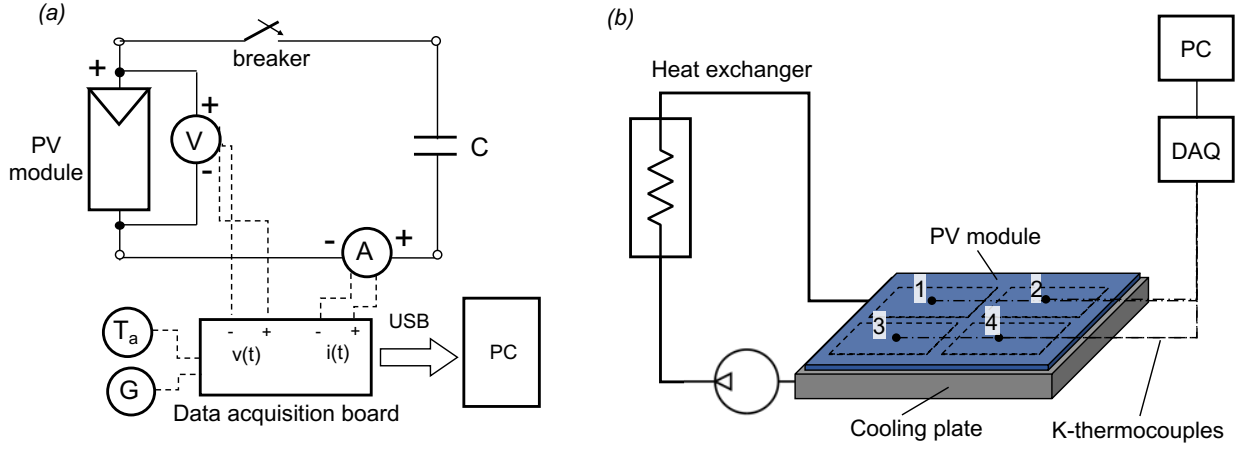
8

Figure 5: Experimental setup used for the outdoor electrical characterization of the PV module. The Automatic Data Acquisition System (ADAS) system allows to (a) measure the solar irradiance I_{rr}, the air temperature T_a, and to get the $I - V$ curves of the PV module. (b) The temperature of the PV cells (namely, $T_{cell,1}$, $T_{cell,2}$, $T_{cell,3}$ and $T_{cell,4}$) are varied using a cooling plate connected to a heat exchanger.

et al. (2018) for details). The specific mass flow rate J through the membrane (with thickness d_m) results to be:

$$J = \frac{m_w \epsilon_m p D_{wa}}{R\bar{T}\tau d_m} \ln\left(\frac{1 - x_w^{int} + \frac{D_{wa}}{D_{wK}}}{1 - x_w^{eva} + \frac{D_{wa}}{D_{wK}}}\right), \quad (4)$$

where the superscript *int* refers to the interface between the membrane and the air gap. Accordingly, the flow through the air gap (with thickness d_a and unitary porosity) (Alberghini et al., 2020):

$$J = \frac{m_w p D_{wa}}{R\bar{T} d_a} \ln\left(\frac{1 - x_w^{cond}}{1 - x_w^{int}}\right). \quad (5)$$

The Fuller equation allows to state that $pD_{wa} = 1.19 \times 10^{-4}\bar{T}^{1.75}$ [Pa m^2 s^{-1}] (Yun et al., 2006; Alkhudhiri et al., 2012). The Knudsen diffusion coefficient of water vapour has the following expression (Khayet and Matsuura, 2011):

$$D_{wK} = \frac{d_p}{3}\sqrt{\frac{8R\bar{T}}{\pi m_w}}, \quad (6)$$

being d_p the average pore diameter of membrane. Finally, the Mackie-Meares equation models the correlation between porosity and tortuosity as (see Supplementary note 3 for further details):

$$\tau = \frac{(2 - \epsilon_m)^2}{\epsilon_m}. \quad (7)$$

Since $x_w \ll 1$, Eq. (4) and (5) can be approximated by a first-order Taylor series, thus resulting as

$$J = K\Delta p_v. \quad (8)$$

The permeability of the membrane (K), which includes the contributions of molecular and Knudsen diffusion, has the following expression (Khayet and Matsuura, 2011; Chiavazzo et al., 2018):

$$K = \frac{m_w}{R\bar{T}}\left(\frac{p_a \tau d_m}{\epsilon_m p D_{wa}} + \frac{3\tau d_m}{\epsilon_m d_p}\sqrt{\frac{\pi m_w}{8R\bar{T}}} + \frac{p_a d_a}{p D_{wa}}\right)^{-1}, \quad (9)$$

where p_a is the partial pressure of air in the membrane pore. The vapour pressure differential is calculated with the Raoult's law $\Delta p_v = a(Y_{eva})p_v(T_{eva}) - p_v(T_{cond})$ (Alkhudhiri et al., 2012), where $p_v(T)$ can be estimated via empirical formulae, e.g. Antoine's correlation. In this case, the chemical activity of the saltwater (mass fraction $Y_{eva} = 0.035$) is equal to $a(Y_{eva}) = 0.978$ (Chiavazzo et al., 2018) (see Supplementary note 3).

The specific heat flux between evaporators and condensers can be estimated by modelling a sensible contribution due to conduction through the layers, and a latent contribution due to water evaporation/condensation (see Supplementary note 3 for further details) (Chiavazzo et al., 2018; Alberghini et al., 2020; Morciano et al., 2020a).

4.2. Numerical models

Numerical models of the developed prototype have been employed to evaluate its performance and to fully characterize the mass and heat transfer phenomena occurring in the device. In detail, three-dimensional Finite Element Method (FEM) models have been implemented in COMSOL Multiphysics®.

The geometry of the simulated system, which includes a portion of PV panel and one distiller, is shown
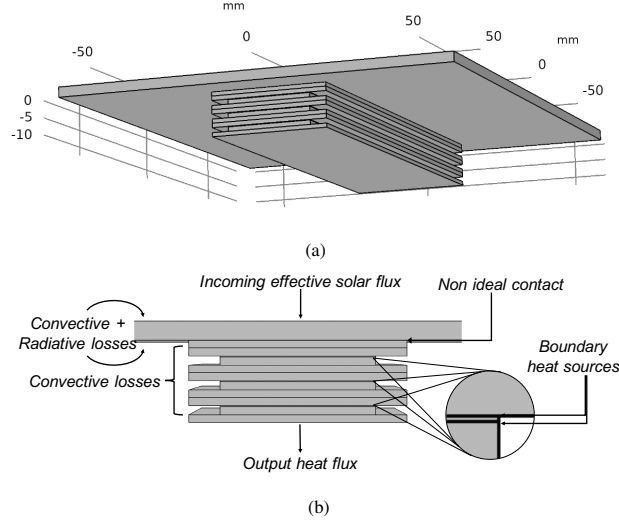
9

Figure 6: FEM model of a representative part of the simultaneous freshwater and electricity production system, consisting of a portion of the PV module and one 3-stage distiller. (a) Geometry and (b) scheme of the applied boundary conditions.

in Fig. 6. On top of the multi-stage distiller, a layer (dimensions: 140 mm × 140 mm × 3 mm) mimicking a PV cell is placed (see Supplementary note 4 for details). Here, a three-stage configuration device is considered, thus the geometry consists of fourteen different blocks, representing the PV cell, the three hydrophobic and porous membranes, the three hydrophilic and porous evaporators, the three hydrophilic and porous condensers and the four aluminium sheets. It is important to notice (see Fig. 6b) the different width between evaporators (35 mm) and condensers (25 mm).

Two sets of equations are solved numerically to obtain the water vapour flux through the membrane and the temperature in the prototype. In detail, the energy conservation and the Fickian convection-diffusion equation for the transport of diluted species are employed. The heat transfer equation is applied throughout the entire computational domain, whilst the transport of diluted species is solved within the domain representing the membranes. It is worth to point out that, in the domains representing all the evaporators and the condensers, Navier-Stokes equations are not solved because of the the negligible velocities due to capillary action. The simulations are performed under stationary regime and a finer mesh calibrated for fluid dynamics is considered. In addition, the *fully coupled* approach is set due to the strong interaction between the various physics involved.

In Figure 6b, the applied boundary conditions are also reported. Boundary heat sources (namely $J\Delta h_{\mathrm{LV}}$, being Δh_{LV} the heat of water vaporization) have been applied

on both sides of the membranes, to model the latent contribution to heat transfer across the membrane. Then, the radiative losses from the boundaries of the PV cell to the ambient are considered, as reported in Fig. 6b. To this purpose, the following equation has been implemented: $-\mathbf{n} \cdot \mathbf{q} = \varepsilon\,\sigma\left(T_{amb}^4 - T^4\right)$, where ε is the surface emissivity, which is equal to 0.95 (see Supplementary Note 4) and σ the Stefan-Boltzmann constant. Finally, the incoming effective solar flux (namely, q_{in}) and the output heat flux exchanged between the heat sink and the environment have been included in the form of appropriate boundary conditions, namely $-\mathbf{n} \cdot \mathbf{q} = q_{in}$ and $-\mathbf{n} \cdot \mathbf{q} = U_{out} \cdot (T_{amb} - T)$, respectively (see Supplementary Note 4 for further details).

A second three-dimensional FEM model is setup to compute the average temperature of the PV cells above the distillers, which allows to estimate the PV efficiency gain. Again, only a representative part of the coupled prototype is simulated. The geometry considers a 140 mm × 140 mm × 3 mm portion of the PV panel (surface slightly larger than that of a single PV cell), while the two distillers in contact with the back side of the PV module are included by means of Neumann boundary conditions. The latter consider the effective thermal transmittance of the distiller – which has been measured as $U_{\mathrm{dist}} = 25.42$ W m^{-2} K^{-1}, the temperature at the boundary – which is the variable for which you are solving, and the known external temperature (see Supplementary note 4).

10

5. Results and discussion

5.1. Distillation performance of a single distiller

The freshwater production of a single distiller under the camouflaged PV panel obtained in the experiments is shown in Fig. 7a, where the mean value $\pm$ 1 s.d. is reported from five different tests, repeated according to the same protocol presented in Section 3.1. When powered with the constant irradiance from sun simulator, the produced distillate increases linearly over time. To monitor the evolution of the performance during the experiments, the specific flow rate of distilled water [L m^{-2} h^{-1}] has been calculated as the volume of distillate generated every 20 minutes normalized by the surface of the condenser cloth (see Fig. 7b). During steady state operation, *i.e.* after 2 hours, the average distillation performance is J_{exp} = 2.03 $\pm$ 0.22 L m^{-2} h^{-1}, in agreement with the results by Wang et al. (2019) for a 3-stage distiller directly exposed to the sun (*i.e.* with no coupling with PV module).

The evolution of temperature profile across the distiller is shown in Fig. 7c. The working temperatures are relatively low, with *Evaporator 1* working at 45 °C ($T_{eva,1}$ = 48.22 °C from numerical simulations) and *Condenser 3* at 22.5 °C ($T_{cond,3}$ = 24.53 °C from numerical simulations). This is mainly due to the heat sink dipped in the saltwater basin at 20 °C, which keeps a lower temperature on the last condenser.

A comparison between the experimental results, the predictions by numerical model and the previous evidence in the literature (Chiavazzo et al., 2018) is shown in Fig. 7d. The average productivity evaluated by the numerical simulations (purple bar) is equal to 2.00 L m^{-2} h^{-1}. The uncertainty of model predictions is quantified by varying the values of the most relevant parameters within realistic intervals. In detail, I_{rr} is affected by the uncertainty due to non-uniformity of the beam, accounting for $\pm$ 51.3 W m^{-2}, namely the standard deviation of the irradiance measured in several points during the calibration of the solar simulator. The convective heat transfer coefficient between the panel and surrounding air is estimated via calculation of natural and forced convection at low air speeds. The thickness of the additional air gap (d_a) between membrane and cloths, which considers their non-ideal contact, ranges from 65 μm to 85 μm. ϵ_m is taken from Chiavazzo et al. (2018); Morciano et al. (2020a). As result, the numerical productivity ranges from 1.41 to 2.76 L m^{-2} h^{-1}, which are the minimum and maximum value evaluated from the combination of values that minimizes and maximizes the productivity, respectively (see Supplementary note

4 for details). The blue bar in Fig. 7d shows the productivity reported by Chiavazzo et al. (2018), that is 1.44 L m^{-2} h^{-1}, from a 3-stage distiller with 0.1 μm microporous membranes tested under one sun. The higher specific distillate flow rate achieved in this work is due to the larger absorbing area of the PV panel, which provides a heat localization effect.

The distillation efficiency of the *j-th* stage of distiller can be expressed as (Chiavazzo et al., 2018):

$$\eta_{dist}(j) = \frac{J(j)\,\Delta h_{LV} A_{cond}}{q_{in} A_{eva}}, \qquad (10)$$

being $J(j)$ the specific distillate flow rate of the *j-th* stage, q_{in} the numerical value of the heat flux that actually passes through the distiller, and A_{cond} = 0.8 $\times$ (125 mm $\times$ 25 mm) = 25 cm^2 and A_{eva} = (125 mm $\times$ 35 mm) = 43.75 cm^2 the effective condenser and evaporator areas, respectively, which are equal for all the stages. Notice that, based on experimental observations, the effective condenser area has been reduced by 20% to consider the portion of the cloth covered by adhesive tape. Instead, the *Gained Output Ratio* (*GOR*) can be used to calculate the overall distillation efficiency as (Lienhard et al., 2017):

$$GOR = \frac{J_{tot}\Delta h_{LV} A_{cond}}{q_{in} A_{eva}}, \qquad (11)$$

being J_{tot} the total distillate flow rate of all the tested stages. The efficiency for the tested 3-stage distiller under the camouflaged PV panel (open circuit) are listed in Table 1, as computed by the validated model. The *GOR* shows the ability of the multi-stage membrane distillation technology to rise the overall efficiency by recovering the latent heat. Notably, the GOR value is about three times the efficiency of the single stages.

Table 1: Specific mass flow rates, efficiency of the *j-th* stage and overall GOR for the 3-stage distiller below the camouflaged PV panel (open circuit) tested under one sun.

	$J(j)$ [L m^{-2} h^{-1}]	$\eta_{dist}(j)$ [%]	GOR [%]
1	0.80	39.80	
2	0.67	32.46	
3	0.53	25.70	
total$_{sim}$	2.00		98.95

The experimental tests show that the solar thermal energy consumption per cubic meter of produced distillate is $(q_{in} A_{eva}) / (\bar{J}_{exp} A_{cond}) \approx 670$ kWh m^{-3}, whilst $\bar{J}_{exp}$ is the average experimental specific mass flow rate. This energy consumption is almost 40% lower with respect
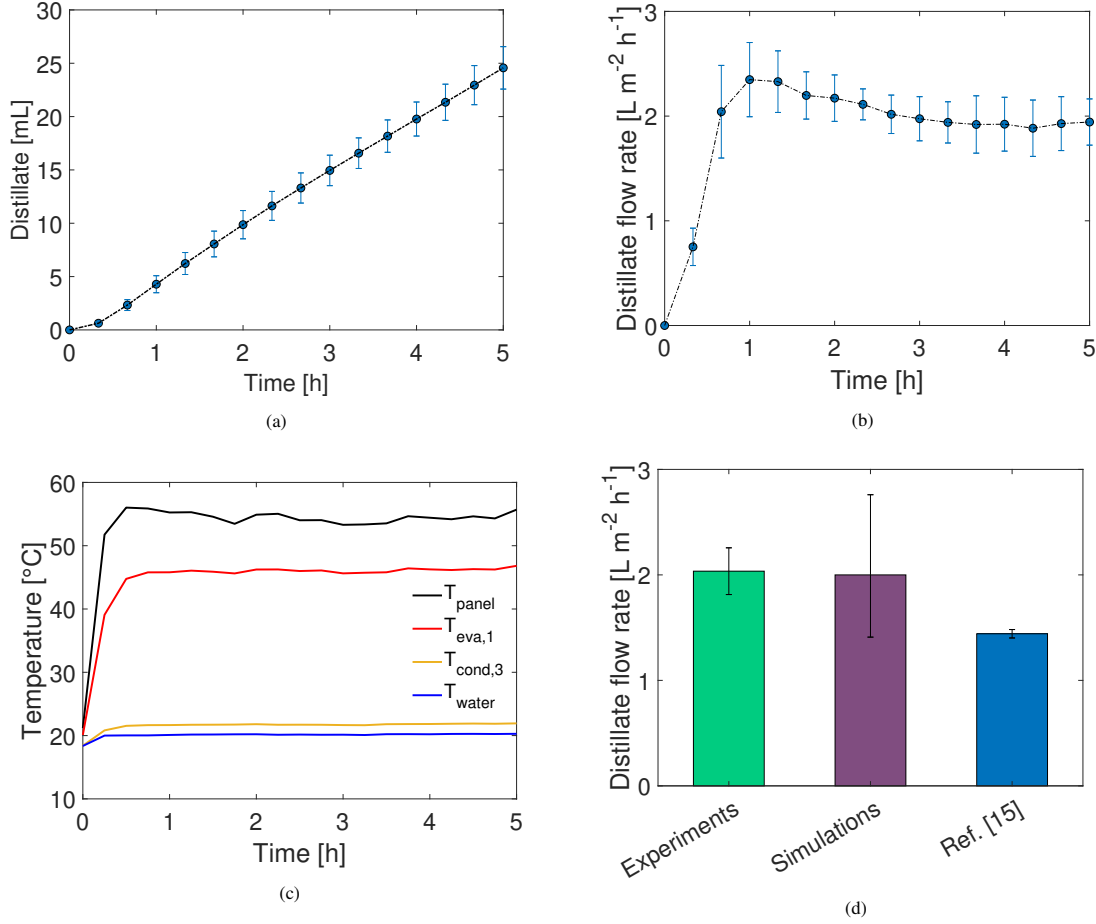
Figure 7: Distillation performance of the system consisting of the camouflaged PV module (open circuit conditions) placed on top of the 3-stage distiller, under reference conditions (I_{rr} = 1000 W m^{-2} and 35 g L^{-1} of NaCl saltwater feed). (a) Produced distillate and (b) its specific flow rate over time; (c) temperature profile over time (uncertainty estimated as: ± 0.2 °C); (d) comparison between the distillation performance obtained from the experiments, numerical simulations and literature (Chiavazzo et al., 2018) (3-stage distiller including a membrane with 0.1 μm pores).

to that of traditional 1-stage solar stills, namely about 1150 kWh m^{-3} (see Supplementary Table S3 by Chiavazzo et al. (2018)). This demonstrates the effectiveness of the multi-stage heat recovery to achieve a more efficient energy management.

5.2. Prototype testing

The full prototype has been tested according to the procedure described in Section 3.2. The net volume of distillate obtained from each distiller in 4 hours under one sun irradiance and the temperature profiles are reported in Figs. 8a and 8b, respectively. All the distillers, except that indicated with G (see also Fig. 4), show a similar overall performance. The average production of distilled water is (18.1 ± 6.4) mL per distiller (including G). The corresponding distillation performance is

J_{exp} = (1.81 ± 0.64) L m^{-2} h^{-1}. If the distiller G is excluded from the calculation – as it is an outlier compared to all other cases – the prototype reaches an average production per distiller equal to (20.3 ± 2.2) mL, which corresponds to $J_{exp,-G}$ = (2.03 ± 0.22) L m^{-2} h^{-1}. These results are coherent with the experiments and numerical simulations shown for a single distiller (see purple bar in Fig. 8a). Finally, at steady state, the experimental temperature of the evaporators (see the red band in Fig. 8b) ranges from 42.7 °C to 47.0 °C, whilst the temperature of the condensers (see the blue band in Fig. 8b) from 22.4 °C to 24.9 °C.

5.3. PV electrical characterization

The $I-V$ curves of the camouflaged PV module have been determined for several temperatures of the cell,
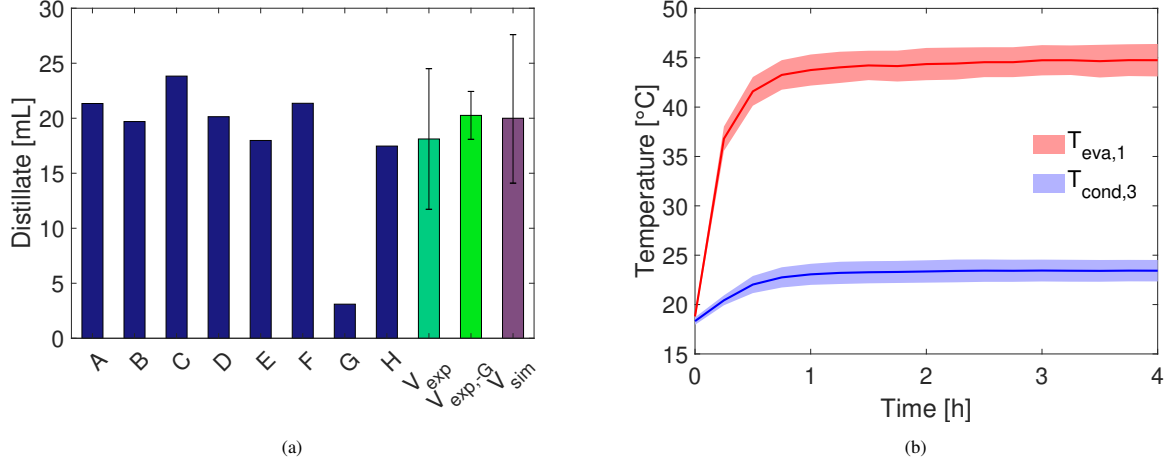
(a)

(b)

Figure 8: Distillation performance of the prototype consisting of eight 3-stage distillers below a camouflaged PV panel (open circuit) under one sun. (a) Overall net production of distillate after 4 h under I_{rr} = 1000 W m^{-2} and with 35 g L^{-1} saltwater salinity. The blue bars show the distillate produced by each of the eight distillers in the prototype (named A–H). The dark green bar shows the average value (±1 s.d.) of distillate produced by the entire prototype, whilst the light green bar shows the average value (±1 s.d.) excluding the distiller G. The purple bar shows the numerical prediction with minimum and maximum values. (b) Evolution of temperature difference between the first evaporators and last condensers of modules A, B, G and H (average ±1 s.d.).

and the results are reported in Fig. 9. The cell temperature T_{cell} ranges from 25.0 °C to 64.0 °C during the outdoor testing. As discussed in Section 3.3 and in Supplementary note 2, variations of T_{cell} impact on V_{oc}, while the effects on the current are negligible. The results confirm this behavior: at T_{cell} = 64 °C the I–V curve presents V_{oc} = 2.24 V, while a reduction of T_{cell} of ≈40 °C leads to V_{oc} = 2.55 V, namely a 14% increase in voltage. In the short circuit region ($I \approx I_{sc}$ and $V \approx 0$ V), the I–V curves present similar short-circuit currents: the differences are due to the marginal variation of irradiance during the measurements. On the contrary, in the open circuit region ($I \approx 0$ A and $V \approx V_{oc}$), the slopes of the I–V curves are negative and they vary according to T_{cell}. In particular, at lower T_{cell}, the curves are steeper, resulting in a higher Fill Factor (Spertino et al., 2015), ranging between 71% and 74% for T_{cell} equal to 64.0 °C and 25.0 °C, respectively.

Regarding the $P - V$ curves, the same considerations can be applied to open-circuit state. Moreover, the T_{cell} reduction of 40 °C allows to increase the PV output power from 6.48 W to 7.77 W, leading to a +20% increase. The temperature coefficients have been evaluated using Eqs. (S1) and (S2) in Supplementary note 2, resulting in γ_{exp} = −0.45 % K^{-1}, and β_{exp} = −0.31 % K^{-1}. These values are in the range generally valid for commercial PV modules. Indeed, the temperature coefficient for power γ ranges between ≈ −0.45 % K^{-1} and ≈ −0.35 % K^{-1} (Schujman et al., 2015; Liu and Dong,

2016), while a common value for β is ≈ −0.3 % K^{-1} (Dubey et al., 2015).

Eventually, the currents have been corrected to Standard Test Conditions (STC, see Supplementary note 2): this correction allows to avoid the effects due to a non-uniform irradiance during the measurements. No correction has been applied to the voltages, in order to evaluate the effect of cell temperature on PV efficiency η_{PV}. Figure 9c shows the efficiency estimated from the experiments (red rhombus), the corrected values (blue squares) and the values calculated with Eq. (S3) using γ_{exp} = −0.45 % K^{-1} and η_{STC} = 12.7%. The corrected data are well represented by Eq. (S3); in particular, η_{PV} increases by 22%, passing from 10.5% (T_{cell} = 64 °C) to 12.7% (T_{cell} = 25 °C).

5.4. PV efficiency enhancement by distiller

The designed and tested prototype is conceived to recover the waste heat from the back side of the camouflaged PV module to feed the distillation process while simultaneously generating electricity. The efficiency of the PV module is also expected to be higher when tested together with the passive membrane desalination device, owing to the resulting reduced temperature of PV cells. The desalination modules, indeed, act as coolers because of their thermal contact with the saltwater reservoir. Here, the evaluation of this expected PV efficiency gain is performed by comparing the temperature of the
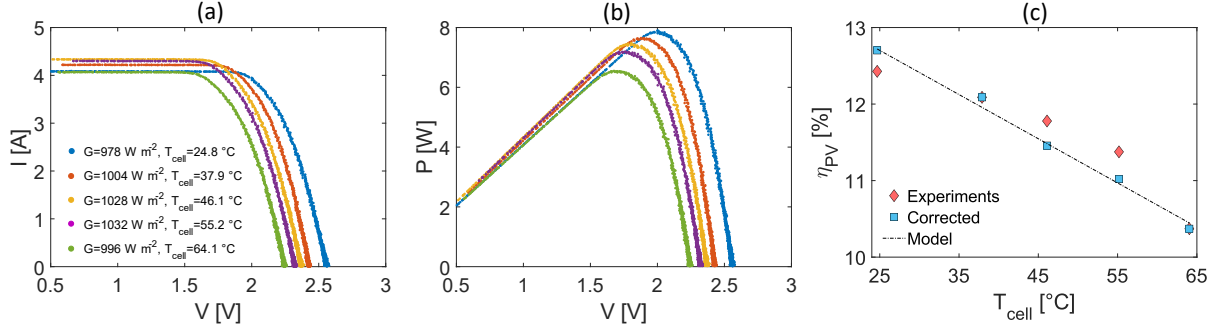
13

Figure 9: Results of the electric PV characterization in outdoor conditions and for different temperatures of the cells. Experimental (a) $I - V$ and (b) $P - V$ charts. In panel (c), the maximum experimental PV efficiencies (red rhombus) are plotted together with their corrected values (blue squares) and the values obtained with the model (black dashed line).

cells when the panel is tested with (T_{cell}) and without ($T_{\text{cell, uncooled}}$) the distillation devices below.

On the one hand, $T_{\text{cell, uncooled}}$ is assessed introducing the PV module alone under the solar simulator (one sun irradiance, open circuit conditions) and measuring the temperature of the four cells on the back side of the module. The experimental average temperature of the four cells is equal to $T_{\text{cell, uncooled}} = 62.4$ °C ($T_{\text{cell, uncooled}} = 64.0$ °C from numerical simulation). In this case, the temperature throughout the module is almost uniform.

On the other hand, the temperature of the cells when the PV module is coupled with the distillers (T_{cell}) is not uniform, as the infrared image in Fig. 10a shows. It is possible to note the colder rectangular areas caused by the two distillers in thermal contact with the back side of the PV cell. During this experiment, temperatures have been measured in the center of the PV cells 1 and 4 (on the back side of the module, see Fig. 4), finding an average value of 60.0 °C in good agreement with that from the numerical simulation in Fig. 10b (61.3 °C). However, the effective operating temperature of the PV cell should be computed as an average value throughout the whole surface of the cell. This can be done by means of the finite-element method model in Fig. 10b, since the average temperature of the PV cell coupled with the two distillers can be estimated from the spatial average of the computed temperature field over the PV cell area. In this configuration, the average temperature of the PV cell has been evaluated numerically as $T_{\text{cell}} = 54.7$ °C. This value represents the expected average temperature of the cells during the synergistic operation with the distillers.

The observed temperature reduction of the cells caused by the cooling effect of distillers should lead to a PV efficiency gain proportional to the temperature coef-

ficient $\gamma_{\text{exp}} = -0.45$ % K^{-1} obtained in Section 5.3, that is

$$\Delta\eta_{\text{PV}} = \frac{\eta_{\text{STC}} \cdot \gamma_{\text{exp}}(T_{\text{cell}} - T_{\text{cell, uncooled}})}{I_{rr}A_{\text{cells}}} = +0.47\%, \tag{12}$$

where $A_{\text{cells}} = 625$ cm^2 is the area of the PV cells in the panel. The maximum power at $T_{\text{cell, uncooled}}$ is $P_{\text{mpp}}(T_{\text{cell, uncooled}}) = 6.6$ W, whilst its efficiency is $\eta_{\text{PV}}(T_{\text{cell, uncooled}}) = 10.56\%$. Then, the relative gain is $\frac{\Delta\eta_{PV}}{\eta_{PV}(T_{cell, uncooled})} = +4.50\%$, which corresponds to an enhanced estimated efficiency $\eta_{\text{PV}}(T_{\text{cell}}) = 11\%$.

These results show the effectiveness of the synergy between the camouflaged PV module and the passive desalination technology. A further enhancement of the PV efficiency gain could be provided by coupling larger distillers that cover all the surface of the cells, in order to further reduce their mean temperature.

5.5. Energy analysis of the coupled system

We evaluate the various energy contributions to the global efficiency of the coupled prototype, in which freshwater and electricity are produced at the same time. The global efficiency considers both the electric power generation and the distillation process. The incoming power is the solar flux collected by the whole surface of the panel, namely $A_{\text{panel}} = 1268$ cm^2. This thermal power is equal to $P_{\text{Irr}} = I_{rr}A_{\text{panel}} = 126.8$ W. The PV cells allow to generate, at MPP (Maximum Power Point of the characteristic $P - V$ curve) and $T_{\text{cell}} = 54.7$ °C, an electric output equal to $P_{\text{mpp}}(T_{\text{cell}}) = 6.9$ W, which corresponds to a PV efficiency of $\eta_{\text{PV}}(T_{\text{cell}}) = 11\%$. To estimate the energy output corresponding to the distillation process, instead, the product of the latent heat of vaporization and the average production rate of distillate from the eight distillers is taken into account via $P_{\text{dist}} = 8 J_{\text{exp}} \Delta h_{\text{LV}} A_{\text{cond}} = 27.2$ W.
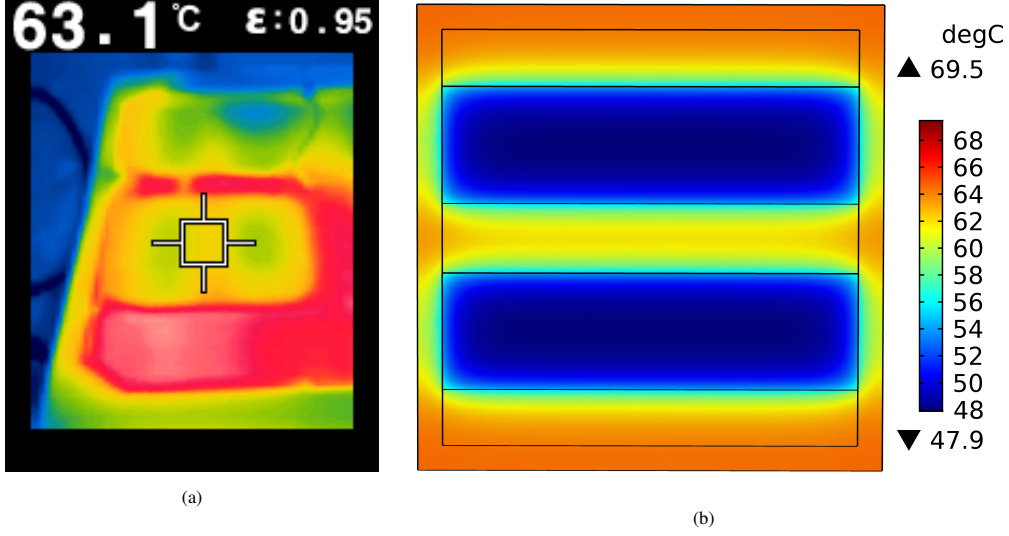
Figure 10: (a) Infrared picture of the surface of the PV module coupled with the distillers during the experiments and the corresponding (b) simulated temperature field from the numerical model.

Since the photovoltaic efficiency is defined as $\eta_{PV} = P_{mpp}/P_{Irr}$, here the potential of the distillers to recover the waste heat from the back side of the PV cells is measured by defining a thermal recovery efficiency:

$$\eta_{Recovery} = \frac{P_{dist}}{P_{Irr}} = 21.46\%. \qquad (13)$$

Eventually, the global efficiency of the prototype, being the sum of the two outputs, is equal to:

$$\eta_{Prototype} = \eta_{Recovery} + \eta_{PV}(T_{cell}) = \qquad (14)$$

$$= \frac{P_{dist} + P_{mpp}(T_{cell})}{P_{Irr}} = 26.90\%. \qquad (15)$$

It is worth to point out that, in this study, the temperature reduction of the PV cells due to their electric connection is considered as negligible, thus not affecting the distillation performance. Whereas, Wang et al. (2019) demonstrated a -9% decrease in productivity for a device consisting of a 3-stage distiller and a PV module operating at maximum power under one sun irradiance.

6. Conclusions

In this work, we have analyzed the coupling between a camouflaged photovoltaic technology and a passive, thermal desalination device. The water treatment unit is mounted on the back side of the PV module, which allows to recover and exploit the waste heat for freshwater production. Overall, the main original contributions of the presented solution are: i) the innovative aesthetic surface coating, which allows to reduce the visual impact on the surrounding landscape; ii) a mosaic-like arrangement of small-sized modular and passive distillers, which eases the scalability of the capillary-driven distillation processes; iii) the enhanced electricity generation efficiency due to the PV cell cooling provided by the distillation device coupled below. Hence, this proof-of-concept prototype results to be a compact and efficient coupled solution for water and energy needs.

Laboratory experiments have shown that, in realistic conditions (solar irradiance equal to 1000 W m^{-2}, saltwater feed temperature and salinity equal to 20 °C and 35 g L^{-1}, respectively), a desalination rate up to 2 L m^{-2} h^{-1} can be achieved. The energy required by the desalination system, around 670 kWh m^{-3}, results to be competitive with other solar desalination techniques (see Supplementary note 5). Moreover, the synergistic integration between the desalination and the PV modules has demonstrated higher electric performance in optimal conditions, thanks to to the lower operating temperature of the PV module. In this sense, a relative PV efficiency gain of 4.50% has been observed when the temperature of the PV cells is decreased by 9 °C.

The adopted desalination technology relies on inexpensive and broadly available materials, and the textured PV module has a reduced visual impact. These choices allow to: i) reduce the costs of the desalination unit for its integration within compact cogenera-

15

tion systems; ii) increase the social acceptance of the installations and their integration with the surrounding landscape (here, particularly thought for floating installations). Based on these considerations, a complete SWOT analysis of the proposed technology (see Supplementary note 6) highlights its high flexibility and applicability to remote and stand-alone installations. However, the proposed solution also shows a few weaknesses: first, the solution still represents a lab-scale prototype with a limited Technology Readiness Level (TRL); second, the visual texture slightly reduces the PV efficiency, and no self cleaning operations from dust are yet proposed or implemented. In perspective, the freshwater productivity could be enhanced by stacking additional distillation stages, while the PV efficiency improved by removing the aesthetic camouflage (if tolerated in the considered installation site).

A scaling-up of the proposed system may be finally envisioned: for example, a 1 m^2 device could potentially provide the basic need of drinkable water for 4 to 5 people per day (*i.e.* $\approx$ 3 L day^{-1} person^{-1} (Institute of Medicine (US). Panel on Dietary Reference Intakes for Electrolytes and Water, 2004)). This may be particularly interesting in off-grid areas in coastal regions or small remote islands.

Acknowledgments

Authors contributions

Conceptualization: M.F.; Methodology: all authors; Software: G.A., M.M.; Formal analysis: all authors; Investigation: G.A., G.M.; Resources: M.A., A.C.; Data Curation: G.A.; Writing - Original Draft: G.A., M.M., G.M.; Writing - Review & Editing: L.B., F.S., M.F.; Visualization: G.A., M.M., G.M.; Supervision: M.F., F.S.

Supplementary material

Supplementary material to this article is available online.

References

Abd Elbar, A.R., Yousef, M.S., Hassan, H., 2019. Energy, exergy, exergoeconomic and enviroeconomic (4e) evaluation of a new integration of solar still with photovoltaic panel. Journal of cleaner production 233, 665–680.

Al-Karaghouli, A., Renne, D., Kazmerski, L.L., 2010. Technical and economic assessment of photovoltaic-driven desalination systems. Renewable Energy 35, 323–328.

Alberghini, M., Morciano, M., Fasano, M., Bertiglia, F., Fernicola, V., Asinari, P., Chiavazzo, E., 2020. Multistage and passive cooling process driven by salinity difference. Science advances 6, eaax5015.

Alkhudhiri, A., Darwish, N., Hilal, N., 2012. Membrane distillation: A comprehensive review. Desalination 287, 2–18.

Bologna, A., Fasano, M., Bergamasco, L., Morciano, M., Bersani, F., Asinari, P., Meucci, L., Chiavazzo, E., 2020. Techno-economic analysis of a solar thermal plant for large-scale water pasteurization. Applied Sciences 10, 4771.

Campione, A., Gurreri, L., Ciofalo, M., Micale, G., Tamburini, A., Cipollina, A., 2018. Electrodialysis for water desalination: A critical assessment of recent developments on process fundamentals, models and applications. Desalination 434, 121–160.

Cazzaniga, R., Cicu, M., Rosa-Clot, M., Rosa-Clot, P., Tina, G., Ventura, C., 2018. Floating photovoltaic plants: Performance analysis and design solutions. Renewable and Sustainable Energy Reviews 81, 1730–1741.

Chen, Q., Burhan, M., Akhtar, F.H., Ybyraiymkul, D., Shahzad, M.W., Li, Y., Ng, K.C., 2021. A decentralized water/electricity cogeneration system integrating concentrated photovoltaic/thermal collectors and vacuum multi-effect membrane distillation. Energy 230, 120852.

Chiavazzo, E., Morciano, M., Viglino, F., Fasano, M., Asinari, P., 2018. Passive solar high-yield seawater desalination by modular and low-cost distillation. Nature sustainability 1, 763–772.

Dao, V.D., Vu, N.H., Dang, H.L.T., Yun, S., 2021. Recent advances and challenges for water evaporation-induced electricity toward applications. Nano Energy , 105979.

De Angelis, P., Tuninetti, M., Bergamasco, L., Calianno, L., Asinari, P., Laio, F., Fasano, M., 2021. Data-driven appraisal of renewable energy potentials for sustainable freshwater production in africa. Renewable and Sustainable Energy Reviews 149, 111414. doi:https://doi.org/10.1016/j.rser.2021.111414.

Dubey, R., Batra, P., Chattopadhyay, S., Kottantharayil, A., Arora, B.M., Narasimhan, K.L., Vasi, J., 2015. Measurement of temperature coefficient of photovoltaic modules in field and comparison with laboratory measurements, in: 2015 IEEE 42nd Photovoltaic Specialist Conference (PVSC), pp. 1–5. doi:10.1109/PVSC.2015.7355852.

Elminshawy, N.A., Gadalla, M.A., Bassyouni, M., El-Nahhas, K., Elminshawy, A., Elhenawy, Y., 2020. A novel concentrated photovoltaic-driven membrane distillation hybrid system for the simultaneous production of electricity and potable water. Renewable Energy 162, 802–817.

Giudici, F., Castelletti, A., Garofalo, E., Giuliani, M., Maier, H.R., 2019. Dynamic, multi-objective optimal design and operation of water-energy systems for small, off-grid islands. Applied Energy 250, 605–616.

Helal, A., Al-Malek, S., 2006. Design of a solar-assisted mechanical vapor compression (mvc) desalination unit for remote areas in the uae. Desalination 197, 273–300.

Institute of Medicine (US). Panel on Dietary Reference Intakes for Electrolytes and Water, 2004. DRI, dietary reference intakes for water, potassium, sodium, chloride, and sulfate. National Academy Press.

Jiang, M., Shen, Q., Zhang, J., An, S., Ma, S., Tao, P., Song, C., Fu, B., Wang, J., Deng, T., et al., 2020. Bioinspired temperature regulation in interfacial evaporation. Advanced Functional Materials 30, 1910481.

Khayet, M., Matsuura, T., 2011. Membrane distillation: principles and applications .

Khayet, M., Sanmartino, J., Essalhi, M., García-Payo, M., Hilal, N., 2016. Modeling and optimization of a solar forward osmosis pilot plant by response surface methodology. Solar Energy 137, 290–302.

Koutroulis, E., Kolokotsa, D., 2010. Design optimization of desalination systems power-supplied by pv and w/g energy sources. Desalination 258, 171–181.

Lee, S., Myung, S., Hong, J., Har, D., 2016. Reverse osmosis desalination process optimized for maximum permeate production with renewable energy. Desalination 398, 133–143.

Letcher, T.M., Fthenakis, V.M., 2018. A Comprehensive Guide to Solar Energy Systems: With Special Focus on Photovoltaic Systems. Academic Press.

Lienhard, J.H., Mistry, K.H., Sharqawy, M.H., Thiel, G.P., 2017. Thermodynamics, exergy, and energy efficiency in desalination systems .

Liu, G., Chen, T., Xu, J., Li, G., Wang, K., 2020. Solar evaporation for simultaneous steam and power generation. Journal of Materials Chemistry A 8, 513–531.

Liu, S., Dong, M., 2016. Quantitative research on impact of ambient temperature and module temperature on short-term photovoltaic power forecasting, in: 2016 International Conference on Smart Grid and Clean Energy Technologies (ICSGCE), pp. 262–266. doi:10.1109/ICSGCE.2016.7876066.

Manokar, A.M., Winston, D.P., Kabeel, A., Sathyamurthy, R., 2018. Sustainable fresh water and power production by integrating pv panel in inclined solar still. Journal of cleaner production 172, 2711–2719.

Morciano, M., Fasano, M., Bergamasco, L., Albiero, A., Curzio, M.L., Asinari, P., Chiavazzo, E., 2020a. Sustainable freshwater production using passive membrane distillation and waste heat recovery from portable generator sets. Applied Energy 258, 114086.

Morciano, M., Fasano, M., Boriskina, S.V., Chiavazzo, E., Asinari, P., 2020b. Solar passive distiller with high productivity and marangoni effect-driven salt rejection. Energy & Environmental Science 13, 3646–3655.

Nassrullah, H., Anis, S.F., Hashaikeh, R., Hilal, N., 2020. Energy for desalination: A state-of-the-art review. Desalination 491, 114569.

Sahu, A., Yadav, N., Sudhakar, K., 2016. Floating photovoltaic power plant: A review. Renewable and sustainable energy reviews 66, 815–824.

Sánchez-Pantoja, N., Vidal, R., Pastor, M.C., 2018. Aesthetic impact of solar energy systems. Renewable and Sustainable Energy Reviews 98, 227–238.

Schujman, S.B., Mann, J.R., Dufresne, G., LaQue, L.M., Rice, C., Wax, J., Metacarpa, D.J., Haldar, P., 2015. Evaluation of protocols for temperature coefficient determination, in: 2015 IEEE 42nd Photovoltaic Specialist Conference (PVSC), pp. 1–4. doi:10.1109/PVSC.2015.7355840.

Signorato, F., Morciano, M., Bergamasco, L., Fasano, M., Asinari, P., 2020. Exergy analysis of solar desalination systems based on passive multi-effect membrane distillation. Energy Reports 6, 445–454.

Solanki, C.S., 2015. Solar photovoltaics: fundamentals, technologies and applications. Phi learning pvt. Ltd.

Spertino, F., Ahmad, J., Ciocia, A., Di Leo, P., Murtaza, A.F., Chiaberge, M., 2015. Capacitor charging method for i–v curve tracer and mppt in photovoltaic systems. Solar Energy 119, 461–473.

Spertino, F., Ciocia, A., Corona, F., Di Leo, P., Papandrea, F., 2014. An experimental procedure to check the performance degradation on-site in grid-connected photovoltaic systems, in: 2014 IEEE 40th Photovoltaic Specialist Conference (PVSC), IEEE. pp. 2600–2604.

Spertino, F., Ciocia, A., Di Leo, P., Fichera, S., Malgaroli, G., Ratclif, A., 2019. Toward the complete self-sufficiency of an nzebs microgrid by photovoltaic generators and heat pumps: Methods and applications. IEEE Transactions on Industry Applications 55, 7028–7040.

Sultan, S.M., Efzan, M.E., 2018. Review on recent photovoltaic/thermal (pv/t) technology advances and applications. Solar Energy 173, 939–954.

UN General Assembly, 2015. Transforming our world: the 2030 Agenda for Sustainable Development.

UNICEF, March 2021. Reimagining WASH: Water Security for All. Technical Report.

Wang, W., Aleid, S., Shi, Y., Zhang, C., Li, R., Wu, M., Zhuo, S., Wang, P., 2021. Integrated solar-driven pv cooling and seawater desalination with zero liquid discharge. Joule .

Wang, W., Shi, Y., Zhang, C., Hong, S., Shi, L., Chang, J., Li, R., Jin, Y., Ong, C., Zhuo, S., et al., 2019. Simultaneous production of fresh water and electricity via multistage solar photovoltaic membrane distillation. Nature communications 10, 1–9.

Xu, H., Ji, X., Wang, L., Huang, J., Han, J., Wang, Y., 2020. Performance study on a small-scale photovoltaic electrodialysis system for desalination. Renewable Energy 154, 1008–1013.

Xue, G., Xu, Y., Ding, T., Li, J., Yin, J., Fei, W., Cao, Y., Yu, J., Yuan, L., Gong, L., et al., 2017. Water-evaporation-induced electricity with nanostructured carbon materials. Nature nanotechnology 12, 317–321.

Yang, P., Liu, K., Chen, Q., Li, J., Duan, J., Xue, G., Xu, Z., Xie, W., Zhou, J., 2017. Solar-driven simultaneous steam production and electricity generation from salinity. Energy & Environmental Science 10, 1923–1927.

Yun, Y., Ma, R., Zhang, W., Fane, A., Li, J., 2006. Direct contact membrane distillation mechanism for high concentration nacl solutions. Desalination 188, 251–262.

Yusuf, A., Sodiq, A., Giwa, A., Eke, J., Pikuda, O., De Luca, G., Di Salvo, J.L., Chakraborty, S., 2020. A review of emerging trends in membrane science and technology for sustainable water treatment. Journal of Cleaner Production , 121867.

Zhang, Y., Zhang, H., Xiong, T., Qu, H., Koh, J.J., Nandakumar, D.K., Wang, J., Tan, S.C., 2020. Manipulating unidirectional fluid transportation to drive sustainable solar water extraction and brine-drenching induced energy generation. Energy & Environmental Science 13, 4891–4902.

Zhou, X., Zhang, W., Zhang, C., Tan, Y., Guo, J., Sun, Z., Deng, X., 2020. Harvesting electricity from water evaporation through microchannels of natural wood. ACS applied materials & interfaces 12, 11232–11239.